

## Multi-scale modeling and simulation of additive manufacturing based on fused deposition technique

F SCI

Cite as: Phys. Fluids **35**, 034116 (2023); <https://doi.org/10.1063/5.0141316>

Submitted: 05 January 2023 • Accepted: 02 March 2023 • Published Online: 21 March 2023

 Qing Xia (夏青),  Gangming Sun (孙港明),  Junseok Kim (김준석), et al.

### COLLECTIONS

 This paper was selected as Featured

 This paper was selected as Scilight



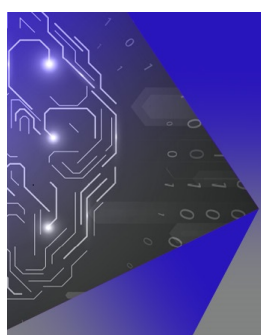
View Online



Export Citation



CrossMark



### APL Machine Learning

Machine Learning for Applied Physics  
Applied Physics for Machine Learning

**First Articles  
Now Online!**

# Multi-scale modeling and simulation of additive manufacturing based on fused deposition technique

F SCI

Cite as: Phys. Fluids 35, 034116 (2023); doi: 10.1063/5.0141316

Submitted: 5 January 2023 · Accepted: 2 March 2023 ·

Published Online: 21 March 2023



View Online



Export Citation



CrossMark

Qing Xia (夏青),<sup>1</sup> Gangming Sun (孙港明),<sup>1</sup> Junseok Kim (김준석),<sup>2</sup> and Yibao Li (李义宝)<sup>1,a)</sup>

## AFFILIATIONS

<sup>1</sup>School of Mathematics and Statistics, Xi'an Jiaotong University, Xi'an 710049, China<sup>2</sup>Department of Mathematics, Korea University, Seoul 02841, South Korea<sup>a)</sup>Author to whom correspondence should be addressed: [yibaoli@xjtu.edu.cn](mailto:yibaoli@xjtu.edu.cn). URL: <http://gr.xjtu.edu.cn/web/yibaoli>

## ABSTRACT

The issue of multi-scale modeling of the filament-based material extrusion has received considerable critical attention for three-dimensional (3D) printing, which involves complex physicochemical phase transitions and thermodynamic behavior. The lack of a multi-scale theoretical model poses significant challenges for prediction in 3D printing processes driven by the rapidly evolving temperature field, including the nonuniformity of tracks, the spheroidization effect of materials, and inter-track voids. Few studies have systematically investigated the mapping relationship and established the numerical modeling between the physical environment and the virtual environment. In this paper, we develop a multi-scale system to describe the fused deposition process in the 3D printing process, which is coupled with the conductive heat transfer model and the dendritic solidification model. The simulation requires a computational framework with high performance because of the cumulative effect of heat transfer between different filament layers. The proposed system is capable of simulating the material state with the proper parameter at the macro- and micro-scale and is directly used to capture multiple physical phenomena. The main contribution of this paper is that we have established a totally integrated simulation system by considering multi-scale and multi-physical properties. We carry out several numerical tests to verify the robustness and efficiency of the proposed model.

Published under an exclusive license by AIP Publishing. <https://doi.org/10.1063/5.0141316>

## I. INTRODUCTION

Extracting additive manufacturing (AM) processes from reality and establishing a corresponding physical model are the significant pursuits during the last decade.<sup>1–4</sup> The AM process is often accompanied by properties of high temperature, high pressure, huge demand for consumables, and high cost, while lacking the ability to predict multiple characteristics, such as nonuniformity of tracks, spheroidization effect of materials, and inter-track voids,<sup>5</sup> which requires the coupling consideration of multi-component systems<sup>6,7</sup> and high-performance computation in non-Euclidean space.<sup>8</sup> Yan *et al.*<sup>9–12</sup> recently completed a series of multi-scale models based on electron beam and substrate interaction. They developed the models based on Monte Carlo simulations, which were capable of accounting for the properties of materials and electron beams. Liu *et al.*<sup>13,14</sup> proposed the particle-based method for selective laser melting of AM, which combined the finite volume method and discrete element method to overcome the challenges of discontinuous physics. Markl and Körner<sup>15</sup> performed a numerical modeling approach on multiple length scales

and timescales for different descriptions of powder bed fusion processes. Geng *et al.*<sup>16</sup> proposed a quantitative phase-field model, which has been widely used in image processing,<sup>17</sup> topology optimization<sup>18,34</sup> to simulate the fused-coating evolution of molten pool, which linked different scales through physical parameters such as temperature gradients and solidification rates. There is no appropriate multi-scale model for modeling the filament-based extrusion with fused deposition (FD) technology.

The FD technique is a melt extrusion AM process driven by high temperature,<sup>19</sup> which provides functional prototypes with the ability to produce complex geometrical parts.<sup>20</sup> The nozzle moves along the path set by the G-code with a given velocity and deposits the filament on the already solidified material,<sup>21</sup> which can be shown schematically in Fig. 1. Anisotropic crystallization is involved in the process of solidification. This technology is widely used in many fields due to its simple process, low cost, and multiple materials [metal, ceramic, poly lactic acid (PLA) plastic, etc.].<sup>22</sup> Despite these advantages, physical models obtained by using the FD technique still presented challenges such as

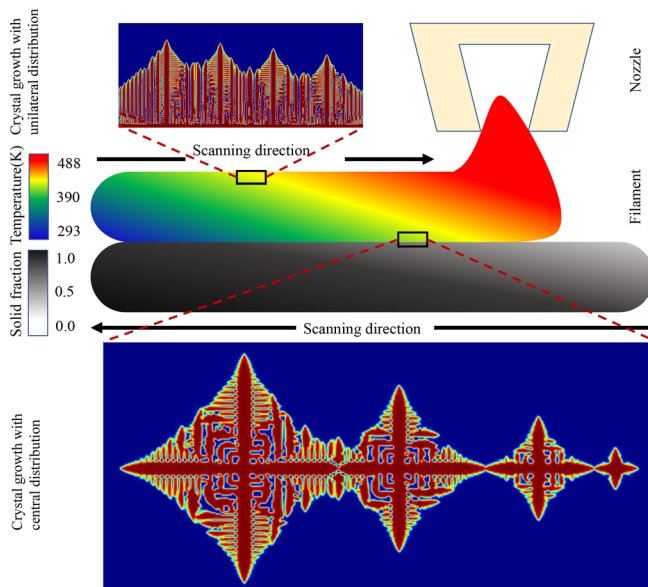


**FIG. 1.** Schematic diagram of manufacturing process involving multi-scale and multi-physical phenomena.

multiple processing parameters, which influenced the mechanical properties, dimensional accuracy, part quality, and production cycle.<sup>23</sup> The main challenges can be summarized as follows: (i) The temperature changes dramatically during the AM process and varies much more slowly than the phase-field in both space and time.<sup>24</sup> (ii) The established model should be used to balance the relationship between the multiple scales,<sup>25</sup> which results in a huge amount of calculation.<sup>26</sup> (iii) The efficiency and relationship between model parameters and manufacturing parameters determine whether the model can accurately predict and feedback to the AM processes.<sup>27,28</sup> Nasirov *et al.*<sup>29</sup> proposed an asymptotic homogenization method to explore the mechanical properties by considering the account of the periodicity and multi-scale nature of infill patterns. Sánchez-Balanzar *et al.*<sup>30</sup> simplified the representative volume elements model and implemented a multi-scale homogenization method for the generation of the unidirectional and criss-cross meso-structures. Xia *et al.*<sup>31,32</sup> focused on the physical behavior and captured some aspects of the full FD process with a meso-scale model, which can be used to examine how the process parameters influence the object during the AM process. Xia *et al.*<sup>33</sup> considered the surface computation from the mesoscopic point of view and established the unconditionally stable numerical scheme to investigate the hydrodynamic behavior. Their study focused on the single scale and mainly contributed to perform the efficient and stable algorithm. For the macro-scale model, Li *et al.*<sup>34</sup> applied the topology optimization approach by considering boundary constraints and physical equation constraints to design macro-structures with personalized differences. However, there are no reference cases of numerical multi-scale modeling for the FD technique during AM processes. In order to reveal the formation mechanism of various defects in the additive manufacturing process and reproduce a series of complex evolutionary processes such as melting, thermodynamical flow, grain growth, and solidification, it is necessary to establish a multi-scale and multi-physical field model to comprehensively consider various physical phenomena.

In this paper, a multi-scale system for the FD technique has been proposed by coupling the conductive heat transfer model and the dendritic solidification model. Compared to our previous studies,<sup>33,34</sup> the novelties of the proposed model in this paper can be summarized as follows: (i) The relationship between multiple scales is comprehensively considered and an integrated system is established. (ii) Focusing on the correspondence between the real additive manufacturing process and the digital model, rather than isolating the physical scene for pure mathematical algorithm research. (iii) The efficient computational scheme is established, which can realize macro–micro synchronous interactive computation. The governing equation obtained by gradient flow under the variational framework is capable of simulating filament-based extrusion of three-dimensional (3D) printing at the macro-scale. Additionally, we consider the temperature field with the moving heat source during AM process. In order to describe the influence brought by the high temperature of the nozzle, we add a thermal convection term coupled with the velocity field of the nozzle to the heat transfer model. The truncated temperature field is used to indicate that the influence of temperature on crystal growth is limited to a certain range.<sup>35</sup> Non-isothermality introduces extra complexity to the polymer dynamics, while semi-crystalline melts will nucleate and crystallize at temperatures below the melting temperature before transitioning to a glassy state.<sup>36</sup> The truncated temperature field is applied in our model as the temperature of crystallization, which is corresponding to the ambient temperature.<sup>37,38</sup> In the mesoscopic case, we focus on the changes in thermal conductivities caused by temperature-induced deformation and consider the anisotropy property of crystal growth at the micro-scale. The proposed model can be used to capture multiple physical phenomena, such as cooling, solidification, crystallization, and deposition of the filament. Meanwhile, under the proposed multi-scale framework, the nonuniformity of tracks, spheroidization effect of materials, and inter-track voids can be easy to make the numerical prediction in AM processes with FD modeling. The originality of this paper is the totally integrated simulation system, which considers the characteristics of different spatial scales to build the corresponding digital model of the real manufacturing process. We efficiently solve the set of equations with the Fourier spectrum method. Although the phase-field crystal equation driven by the rapidly evolving temperature field has strong nonlinearity and intricate coupling relations, our method makes the complicated system well-determined with a stable structure and removes the oscillations caused by the anisotropic properties.

The outline of this paper are as follows. In Sec. II, we introduce the multi-scale governing equations. In Sec. III, the numerical scheme has been established. Section IV is devoted to present various numerical experiments. Finally, concluding remarks are drawn in Sec. V.

## II. MULTI-SCALE GOVERNING EQUATIONS

To begin with the model, let us introduce the Lyapunov type<sup>39</sup> energy functional

$$\mathcal{E}(\phi) = \int_{\Omega} \frac{|\nabla \phi|^2}{2} + \frac{F(\phi)}{\varepsilon^2} + \frac{1}{\varepsilon^2} \lambda \theta \left( \phi - \frac{2\phi^3}{3} + \frac{\phi^5}{5} \right) dx, \quad (1)$$

where  $\phi(x, y, z, t) \in \Omega$  denotes the density field and  $\Omega \subset \mathbb{R}^{\text{dim}}$ , ( $\text{dim} = 2, 3$ ) is the computational domain. We use  $F(\phi) = (\phi^2 - 1)^2/4$  to denote the double-well potential, which obtains minima with  $\phi = \pm 1$ . The positive parameter  $\varepsilon$  is temperature related which controls the width of the diffusive interface,<sup>40</sup> and  $\lambda$  is a dimensionless

parameter that implies the strength of the coupling between the phase field and conductive temperature field.<sup>41</sup> Here,  $\theta$  is the dimensionless temperature, which provides the thermal energy for solidification and encourages crystal growth. By applying the variational derivative on the free energy, one can derive the crystal growth functional as

$$\frac{\partial \phi}{\partial t} = -\frac{\delta \mathcal{E}}{\delta \phi} = \Delta \phi + \frac{1}{\varepsilon^2} (\phi - \lambda \theta (1 - \phi^2)) (1 - \phi^2). \quad (2)$$

Considering that AM is a process of adding materials to the system with the movement of the nozzle and gradually cooling by thermal diffusion, the governing equations are designed to be highly coupled with the symbiotic association as follows:

$$\varepsilon^2 \frac{\partial \phi}{\partial t} = \varepsilon^2 \Delta \phi + (\phi - \lambda \theta (1 - \phi^2)) (1 - \phi^2) + S, \quad (3a)$$

$$\nabla \cdot \left( \frac{k}{\rho C_p} \nabla T \right) + \frac{q(x, y, z, t)}{\rho C_p} = \frac{\partial T}{\partial t} + \mathbf{v}_p \cdot \nabla T, \quad (3b)$$

where  $\phi = 1$  and  $\phi = -1$  refer to the bulk solid and melt phases of the solidification system, respectively. Here,  $T$  is the transient temperature over the object and the dimensionless temperature is computed as

$$\theta = C_p(T - T_M)/L, \quad (4)$$

where  $T_M$  is the ambient temperature,  $L$  is the latent heat coefficient of fusion, and  $C_p$  is the specific heat coefficients. It is worth pointing out that the phase-field variable  $\phi$  is a hyperbolic tangent profile with small constant thickness  $\varepsilon$  across the interfacial transition region.<sup>42</sup> We define the interface of the numerical model by the zero-level set of  $\phi$ . Since the FD technology involves complicated physical behaviors such as the melting process by dramatical temperature, the solidification by the heat diffusion, and chemical reaction by the crystallization, we apply the crystal growth function equation (3a) to construct the physical phenomenon during the AM process. The volume and shape change with the material state, which is not ignored in our model.  $S$  is the amount of nozzle extrusion per unit of time. We should remark that the nozzle moves with a given velocity along with the processed G-code, which can control the extrusion rate, moving path, velocity, and location. Therefore, the volume source can be treated as a sphere at the location  $\mathbf{x}_S$  with a constant volume. We assume that the nominal diameter of the deposited filament  $D = \sqrt{4Q/(\mathbf{v}_s \pi)}$ , where  $Q$  is the feed rate and  $\mathbf{v}_s$  is the velocity of polymer melts leaving the nozzle.

The heat mainly released by the filament extruded from the nozzle during solidification, we cannot neglect to introduce a convective term into the thermal diffusion equation,  $\mathbf{v}_p \cdot \nabla T$ , to consider the influence brought by filament extraction from the nozzle, where  $\mathbf{v}_p$  is the scanning speed of the printer nozzle with moving heat source. Furthermore,  $q$  is the heat source due to the addition of the hot molten polymer of Eq. (3b), which can be defined as

$$q = \rho C_p T_{\text{inj}} S \delta(\mathbf{x} - \mathbf{x}_S). \quad (5)$$

Here,  $T_{\text{inj}}$  is the injection temperature caused by the motion of the nozzle. We consider a dynamic control strategy to describe the relationship between  $T_{\text{inj}}$  and  $\mathbf{v}_p$  of the nozzle as

$$[T_{\text{inj}}] = [\mathbf{v}_p] \frac{\partial T_{\text{inj}}}{\partial \mathbf{v}_p}, \quad (6)$$

where  $[T_{\text{inj}}]$  is the deviation between the maximum value of the  $T_{\text{inj}}$  and the target temperature value. Here,  $[\mathbf{v}_p]$  is the adjusted difference of the scanning speed of the nozzle. Refer to Ref. 43, the mapping function was established experimentally as

$$T_{\text{inj}} = A_s \exp \left( -\frac{\mathbf{v}_p}{B_s} \right) + C_s, \quad (7)$$

where  $A_s$ ,  $B_s$ , and  $C_s$  are the coefficients that depend on the manufacturing mode and relate to the fused region. Let us use  $\delta$  to denote the three-dimensional delta function constructed by repeated multiplication of one-dimensional delta functions, identifying the interface locations.<sup>21</sup> This term considers the heat emitted during the physical state transition of the material after extruding from the nozzle. The different material properties density  $\rho$ , the specific heat capacity of the material  $c$ , and the thermal conductivity  $k$  of the whole system are taken to vary with  $\phi$  and can be defined as follows:

$$\rho(\phi) = \frac{1}{2} (\rho_1(1 + \phi) + \rho_2(1 - \phi)), \quad (8a)$$

$$C_p(\phi) = \frac{1}{2} (C_{p1}(1 + \phi) + C_{p2}(1 - \phi)), \quad (8b)$$

$$k(\phi) = \frac{1}{2} (k_1(1 + \phi) + k_2(1 - \phi)), \quad (8c)$$

where  $\rho_1$  and  $\rho_2$  denote the densities of polymer and air,  $C_{p1}$  and  $C_{p2}$  denote their specific heat coefficients, and  $k_1$  and  $k_2$  denote their thermal conductivities, respectively.

The density and heat capacity of the material is temperature independent, while the thermal conductivity  $k$  at the mesoscale no longer depends only on the materials, but also on the nominal diameters of the filaments and contact area of the interfaces. The purpose of this discussion at the mesoscale is to compensate for the missing convective heat transfer by modifying the thermal conductivity refer to Ref. 44. We neglect the interface resistance and heat accumulation. Heat diffuses unhindered across the gap as the deposition of the hot filaments with the conductivity as

$$k_{\text{meso}} = \frac{4H_{\text{flux}}}{\pi D \times T_{\text{grad}}}, \quad (9)$$

where  $T_{\text{grad}}$  is the temperature gradient and  $H_{\text{flux}}$  is the total heat flux caused by  $T_{\text{grad}}$ . Considering the manufacturing material per unit volume, we integrate the heat flux with respect to the temperature gradient along the boundary. Since only single material is considered in the proposed model, the contact area is symmetric on both sides, which leads to the same thermal conductivity.

Based on the micro-scale perspective, we extend the anisotropic properties to macro-scale model [Eqs. (3)]. Let us replace the constant mobility  $\varepsilon$  with an anisotropic function  $\varepsilon(\phi)$  in the model equation (3a) and modified equation (3b) as follows:<sup>45</sup>

$$\begin{aligned} \varepsilon^2(\phi) \frac{\partial \phi}{\partial t} &= \nabla \cdot (\varepsilon^2(\phi) \nabla \phi) + (\phi - \lambda \theta (1 - \phi^2)) (1 - \phi^2) \\ &+ \tilde{S} + \left( |\nabla \phi|^2 \varepsilon(\phi) \frac{\partial \varepsilon(\phi)}{\partial \phi_x} \right)_x + \left( |\nabla \phi|^2 \varepsilon(\phi) \frac{\partial \varepsilon(\phi)}{\partial \phi_y} \right)_y \\ &+ \left( |\nabla \phi|^2 \varepsilon(\phi) \frac{\partial \varepsilon(\phi)}{\partial \phi_z} \right)_z, \end{aligned} \quad (10a)$$

$$\frac{\partial T}{\partial t} = \nabla \cdot \left( \frac{k}{\rho C_p} \nabla T \right) + \frac{1}{2} \frac{\partial \varphi}{\partial t}, \quad (10b)$$

where  $\varphi(x, y, z)$  represents the phase field variable in the micro-scale and  $\tilde{S} = 6S/\pi D^3$  is the dynamic growth of the material in the microscopic state. Here we take an example with fourfold anisotropy, which implies the anisotropic function as

$$\varepsilon(\varphi) = (1 - 3\tilde{\varepsilon}) \left( 1 + \frac{4\tilde{\varepsilon}}{1 - 3\tilde{\varepsilon}} \frac{\varphi_x^4 + \varphi_y^4 + \varphi_z^4}{|\nabla \varphi|^4} \right), \quad (11)$$

where  $\tilde{\varepsilon}$  is the parameter for the anisotropy strength and  $\varphi_x$ ,  $\varphi_y$ , and  $\varphi_z$  denotes the partial derivative along to  $x$ -,  $y$ -, and  $z$ -direction, respectively. The critical test of this model against the microscopic theory about linear axisymmetric solvability and nonlinear axisymmetric solvability<sup>46</sup> were presented in Ref. 47. The dendrite growth of micro-structure deformation on the boundary and the bond of filaments have been captured by the proposed method and shown in Fig. 1.

Some notations should be summarized as follows: (i) Neither evaporation nor the subsequent mass loss was considered in our model because evaporation is not the concern of this study. Therefore, the latent heat of melting was included; however, the latent heat of vaporization was ignored. Considering that the proposed model is designed for the FD manufacturing process, which involves a phase transition from the viscous liquid state to the solid state, we introduce a coefficient of latent heat  $L$  in Eq. (4) to reduce the computational burden. (ii) We have considered the convective heat transfer by applying the term  $\mathbf{v}_p \cdot \nabla T$  in the macroscopic model equation (3), which is caused by the nozzle movement. However, the convective effect can be neglected in the microscopic model equation (10) since the crystallization is transient on a macroscopic timescale. (iii) The radiative heat transfer on the surface of filaments has to be simplified refer to the extensive work.<sup>10</sup> During the printing process of filament, the temperature reaches several hundred degrees, thereby the convective and radiative heat transfer from the filament to the ambient could be ignorable. Thus we only need to consider the radiative heat transfer between different filaments from the mesoscopic point of view. We modified the thermal conductivity  $k$  in the macro-scale model equation (3) to  $k_{\text{meso}}$  as defined in Eq. (9). It should be mentioned that the surface radiation is small enough to be negligible when calculating the effective thermal conductivity. (iv) Although the mesoscopic and microscopic scale model can reveal the basic physical mechanism and make more accurate predictions, the huge computational burden and high difficulty in building the mathematical model make them unable to be well applied in industrial production. Our multi-scale model aims to provide a research tool, and there are still many physical mechanisms to be explored and explored by using the tools provided in this paper. Furthermore, the established model can also be used to investigate the sensitivity of the forming process and forming quality to some influencing factors, and then ignore the less sensitive influencing factors in the model to simplify the model.

### III. MULTI-SCALE NUMERICAL SOLUTIONS

The numerical solution of our multi-scale system is discretized with the uniform mesh grid. We present the numerical method in two dimension, which can be extended to three dimension in a straightforward manner without loss of generalities. Let us denote

$\Omega^{\text{Ma}} = [L_x^b, L_x^e] \times [L_y^b, L_y^e]$  and  $\Omega^{\text{Mi}} = [l_x^b, l_x^e] \times [l_y^b, l_y^e]$  as the computational domain with a  $N_x^{\text{Ma}} \times N_y^{\text{Ma}}$  and  $N_x^{\text{Mi}} \times N_y^{\text{Mi}}$  mesh-grid in macro-scale and micro-scale, respectively. The center of each macro-cell  $\Omega_{ij}^{\text{Ma}}$  is located at  $\mathbf{x}_{ij}^{\text{Ma}} = (x_i^{\text{Ma}}, y_j^{\text{Ma}}) = (L_x^b + (i - \frac{1}{2})h^{\text{Ma}}, L_y^b + (j - \frac{1}{2})h^{\text{Ma}})$ , where we denote  $h^{\text{Ma}} = (L_x^e - L_x^b)/N_x^{\text{Ma}} = (L_y^e - L_y^b)/N_y^{\text{Ma}}$  as the macro-spatial step for  $i = 1, \dots, N_x^{\text{Ma}}$  and  $j = 1, \dots, N_y^{\text{Ma}}$ . The center of each micro-cell  $\Omega_{sw}^{\text{Mi}}$  is located at  $\mathbf{x}_{sw}^{\text{Mi}} = (x_s^{\text{Mi}}, y_w^{\text{Mi}}) = (l_x^b + (s - \frac{1}{2})h^{\text{Mi}}, l_y^b + (w - \frac{1}{2})h^{\text{Mi}})$ , where we denote  $h^{\text{Mi}} = (l_x^e - l_x^b)/N_x^{\text{Mi}} = (l_y^e - l_y^b)/N_y^{\text{Mi}}$  as the micro-spatial step for  $s = 1, \dots, N_x^{\text{Mi}}$  and  $w = 1, \dots, N_y^{\text{Mi}}$ . Let  $((\cdot)^{\text{Ma}})_{ij}^n$  be approximations of  $(\cdot)^{\text{Ma}}(x_i^{\text{Ma}}, y_j^{\text{Ma}}, n\Delta t^{\text{Ma}})$  and  $((\cdot)^{\text{Mi}})_{sw}^m$  be approximations of  $(\cdot)^{\text{Mi}}(x_s^{\text{Mi}}, y_w^{\text{Mi}}, m\Delta t^{\text{Mi}})$ , where  $\Delta t^{\text{Ma}} = T^{\text{Ma}}/N_t^{\text{Ma}}$  is the macro-time step,  $\Delta t^{\text{Mi}} = T^{\text{Mi}}/N_t^{\text{Mi}}$ ,  $T^{\text{Ma}}$  is the macro-final time and  $T^{\text{Mi}}$  is the micro-final time.

#### A. Macro-scale formulation

Our macro-scale formulation has been computed based on the pressure correction method.<sup>48</sup> The governing system equation (3) can be discretized as

$$\begin{aligned} \nabla_d \cdot \left( \left( \frac{\tilde{k}^{n+1}}{\tilde{\rho}^{n+1}\tilde{C}_p^{n+1}} - M_0 \right) \nabla_d \tilde{T}^{n+1} \right) + M_0 \Delta_d T^{n+1} \\ + \frac{q^{n+1}}{\tilde{\rho}^{n+1}\tilde{C}_p^{n+1}} = \frac{T^{n+1} - T^n}{\Delta t} + \mathbf{v}_p \cdot \nabla_d \tilde{T}^{n+1}, \end{aligned} \quad (12a)$$

$$\begin{aligned} \varepsilon(\tilde{\phi}^{n+1})^2 \frac{\phi^{n+1} - \phi^n}{\Delta t} = \varepsilon(\tilde{\phi}^{n+1})^2 \Delta_d \phi^{n+1} + \phi^{n+1} \\ + G(\phi^{n+1}) - \lambda \theta^{n+1} + S, \end{aligned} \quad (12b)$$

where  $M_0 = \min(\tilde{k}^{n+1}/(\tilde{\rho}^{n+1}\tilde{C}_p^{n+1}))$ ,  $\theta^{n+1} = \tilde{C}_p^{n+1}(T^{n+1} - T_M)/L$ , and  $(\cdot)^{n+1} = 2(\cdot)^n - (\cdot)^{n-1}$ . Here, we use the first-order Taylor expansion for  $G(\phi^{n+1})$  as

$$\begin{aligned} G(\phi^{n+1}) = -4\lambda\theta^{n+1}(\phi^n)^3 + 3(\phi^n)^2 - 4\lambda\theta^{n+1}\phi^n \\ + 3\lambda\theta^{n+1}(\phi^n)^4 + 2(\phi^n)^3 - 2\lambda\theta^{n+1}(\phi^n)^2. \end{aligned}$$

To simplify our presentation, we denote  $G(\phi^{n+1}) = \mathcal{A}\phi^{n+1} + \mathcal{B}$ , where  $\mathcal{A} = 4\lambda\theta^{n+1}(\phi^n)^3 + 3(\phi^n)^2 - 4\lambda\theta^{n+1}\phi^n$  and  $\mathcal{B} = 3\lambda\theta^{n+1} \times (\phi^n)^4 + 2(\phi^n)^3 - 2\lambda\theta^{n+1}(\phi^n)^2$ . The density, specific heat coefficient, and thermal conductivities can be computed at time level  $n+1$  as

$$\rho^{n+1} = 0.5(\rho_1(1 + \phi^{n+1}) + \rho_2(1 - \phi^{n+1})), \quad (13a)$$

$$C_p^{n+1} = 0.5(C_{p1}(1 + \phi^{n+1}) + C_{p2}(1 - \phi^{n+1})), \quad (13b)$$

$$k^{n+1} = 0.5(k_1(1 + \phi^{n+1}) + k_2(1 - \phi^{n+1})). \quad (13c)$$

To compensate for the missing convective heat transfer by modifying the thermal conductivity, we approximate the influence of the effective thermal conductivity by ignoring the surface radiation theoretically. The thermal energy through surface radiation can be computed by

$$H_{\text{flux}} = \pi D^2 \sigma (T_2^4 - T_1^4)/2, \quad (14)$$

where  $\sigma$  is the Stefan–Boltzmann constant.<sup>10</sup> Here, we denote  $T_1$  and  $T_2$  ( $T_1 \leq T_2$ ) to represent the temperatures of the adjacent filaments. According to Eq. (9), we modify the maximum effective thermal conductivity  $k_{\text{meso}}$  at mesoscale as

$$k_{\text{meso}}^{n+1} = \frac{4H_{\text{flux}}^{n+1}}{\pi D^2(T_2^{n+1} - T_1^{n+1})} = \frac{2\sigma((T_2^{n+1})^4 - (T_1^{n+1})^4)}{T_2^{n+1} - T_1^{n+1}}. \quad (15)$$

Considering the balance between computational quantity and computational efficiency, we implement the parallel fast Poisson solver. Let us denote

$$\begin{aligned} UT &= \nabla_d \cdot \left( \left( \left( \frac{\tilde{k}^{n+1}}{\tilde{\rho}^{n+1} C_p^{n+1}} - M_0 \right) \nabla_d \tilde{T}^{n+1} \right) \right. \\ &\quad \left. + \frac{q^{n+1}}{\tilde{\rho}^{n+1} C_p^{n+1}} - \frac{T^{n+1} - T^n}{\Delta t} + \mathbf{v}_p \cdot \nabla_d \tilde{T}^{n+1}, \right) \quad (16) \end{aligned}$$

$$UP = \mathcal{B} - \lambda \theta^{n+1} + S, \quad (17)$$

by rearranging the formulas, we can get the following linearly decoupled system:

$$T^{n+1} = (\mathcal{I} - \Delta t M_0 \mathcal{L})^{-1} (\Delta t UT + T^n), \quad (18a)$$

$$\begin{aligned} \phi^{n+1} &= \left( \left( 1 - \frac{\Delta t}{\varepsilon(\tilde{\phi}^{n+1})^2} \right) \mathcal{I} - \frac{\Delta t \mathcal{A}}{\varepsilon(\tilde{\phi}^{n+1})^2} - \Delta t \mathcal{L} \right)^{-1} \\ &\quad \times \left( \frac{UP}{\varepsilon(\tilde{\phi}^{n+1})^2} + \phi^n \right), \quad (18b) \end{aligned}$$

where  $\mathcal{I}$  and  $\mathcal{L}$  are the identity matrix and the Laplace matrix. Thus, the discrete system leads to the linear, decoupled elliptic equations for the computation, which allows us to solve the temperature field and phase-field separately at each time step. We take the computation of Eq. (18a) as an example to illustrate our algorithm, which can be applied for Eq. (18b) in the same manner. The outline of the macro-scale algorithm is as follows:

- $\mathcal{S}1$ . Initialize  $T^0$  to be the ambient temperature field for the AM process (or  $\phi^0$  to be the equilibrated composition profile).
- $\mathcal{S}2$ . Implement the FFT algorithm in the  $x$ -direction to the right sides of Eq. (18a) [or Eq. (18b)].
- $\mathcal{S}3$ . The 3D complex data obtained by  $\mathcal{S}2$  is transposed between computing cores to distribute the resulting data in the  $x$ -direction and be contiguous in the  $y$ - and  $z$ -directions.
- $\mathcal{S}4$ . Implement  $\mathcal{S}2$  and  $\mathcal{S}3$  alternately in three directions and obtain  $T^{n+1}$  (or  $\phi^{n+1}$ ) in the Fourier space.
- $\mathcal{S}5$ . Implement the inverse FFT algorithm in the  $x$ -direction of 3D data obtained by  $\mathcal{S}4$ .
- $\mathcal{S}6$ . The 3D complex data obtained by  $\mathcal{S}4$  are transposed between computing cores to distribute the resulting data in the  $x$ -direction and be contiguous in the  $y$ - and  $z$ -directions.
- $\mathcal{S}7$ . Implement  $\mathcal{S}5$  and  $\mathcal{S}6$  alternately in three directions and obtain  $T^{n+1}$  (or  $\phi^{n+1}$ ).

## B. Micro-scale formulation

We introduce the two auxiliary variables  $M(\varphi)$  and  $Z(\varphi)$ , which are composed of the phase variable and used to aid the computation.

We perform the Invariant Energy Quadratization (IEQ) method<sup>19</sup> to transform our original micro-scale system. It is worth noting that the two intermediate auxiliary variables have been introduced to transform the governing system into a linear, decoupled form and transform the free energy into a quadratic form, which allows the nonlinear potential to be treated semi-explicitly. Meanwhile, the discrete system can be proved to be unconditionally energy stable, which implies that a larger time step can be used for computation. The new system still retains a similar energy dissipation law in terms of the auxiliary variables  $M(\varphi)$  and  $Z(\varphi)$ . The micro-scale formulation can be summarized as

$$\varepsilon^2(\varphi) \varphi_t = -Z(\varphi) M(\varphi) - \frac{\lambda}{\varepsilon(\varphi)} \theta(1 - \varphi^2)^2 + \tilde{S}, \quad (19a)$$

$$M_t(\varphi) = \frac{1}{2} Z(\varphi) \varphi_t, \quad (19b)$$

$$T_t = \nabla \cdot \left( \frac{k}{\rho C_p} \nabla T \right) + \varepsilon(\varphi) (1 - \varphi^2)^2 \varphi_t, \quad (19c)$$

where

$$Z(\varphi) = \frac{-\nabla \cdot (\varepsilon^2(\varphi) \nabla \varphi + \varepsilon(\varphi) |\nabla \varphi|^2 \mathbf{H}(\varphi)) + f(\varphi)/\varepsilon^2(\varphi)}{\sqrt{|\varepsilon(\varphi) \nabla \varphi|^2/2 + F(\varphi)/\varepsilon^2(\varphi) + B}}, \quad (20a)$$

$$\begin{aligned} \mathbf{H}(\varphi) &= \frac{16\tilde{\varepsilon}}{|\nabla \varphi|^6} \left( \varphi_x \left( \varphi_x^2 \varphi_y^2 + \varphi_x^2 \varphi_z^2 - \varphi_y^4 - \varphi_z^4 \right), \right. \\ &\quad \varphi_y \left( \varphi_y^2 \varphi_z^2 + \varphi_x^2 \varphi_y^2 - \varphi_x^4 - \varphi_z^4 \right), \\ &\quad \left. \varphi_z \left( \varphi_x^2 \varphi_z^2 + \varphi_y^2 \varphi_z^2 - \varphi_x^4 - \varphi_y^4 \right) \right), \quad (20b) \end{aligned}$$

$$M(\varphi) = \sqrt{|\varepsilon(\varphi) \nabla \varphi|^2/2 + F(\varphi)/\varepsilon^2(\varphi) + B}, \quad (20c)$$

where  $B$  is a positive constant, which is necessary for the free energy to be physically sound. It should be pointed out that the time scales of macro-formulation and micro-formulation is not consistent. Since the temperature fluctuations of the system are mainly caused by the filament extraction at the macro-scale, which buries the temperature disturbance effect caused by the crystallization at the micro-scale. Once the temperature field has been obtained by Eq. (18a), the crystallization with anisotropy properties can be computed by Eq. (19) with the following discrete system:

$$\begin{aligned} &\varepsilon^2(\tilde{\varphi}^{n+1}) \frac{3\phi^{n+1} - 4\phi^n + \phi^{n-1}}{2\Delta t} \\ &= -Z(\tilde{\varphi}^{n+1}) \theta^{n+1} - \frac{\lambda}{\varepsilon(\tilde{\varphi}^{n+1})} (1 - (\tilde{\varphi}^{n+1})^2)^2 \theta^{n+1}, \quad (21a) \end{aligned}$$

$$3M^{n+1} - 4M^n + M^{n-1} = \frac{1}{2} Z(\tilde{\varphi}^{n+1}) (3\tilde{\varphi}^{n+1} - 4\tilde{\varphi}^n + \tilde{\varphi}^{n-1}), \quad (21b)$$

$$\begin{aligned} &\frac{3T^{n+1} - 4T^n + T^{n-1}}{2\Delta t} \\ &- \nabla_d \cdot \left( \left( \frac{k^{n+1}}{\rho^{n+1} C_p^{n+1}} - M_0 \right) \nabla_d \tilde{T}^{n+1} \right) + M_0 \Delta_d T^{n+1} \\ &= \varepsilon(\tilde{\varphi}^{n+1}) (1 - (\tilde{\varphi}^{n+1})^2)^2 \times \frac{3\tilde{\varphi}^{n+1} - 4\tilde{\varphi}^n + \tilde{\varphi}^{n-1}}{2\Delta t} \quad (21c) \end{aligned}$$

**Remark 1.** We should point out that we have used the second-order time derivative scheme [Eq. (21)] in the micro-scale case and the first-order time derivative scheme [Eq. (12)] in the macro-scale case. Considering the trade-off between sufficient accuracy and computational complexities, we have to choose different strategies for different scale spaces. From the macroscopic point of view, the first-order accuracy of the temporal scheme is sufficient to simulate the manufacturing process without computational burden. From the microscopic point of view, we apply the unconditionally stable temporal scheme by the IEQ method, which implies that we can choose the large time step for simulation. However, the accuracy of the time integration decreases with the large time step. To overcome the accuracy challenge, we have to abandon the advantages of low computational complexity and select the second-order scheme for the time derivative in the micro-scale model.

The flow chart of the proposed method has been shown in Fig. 2. The pre-processing is used to parse the G-code. The first stage is for the macro-scale computation and the second stage is for the micro-

scale computation. The temperature field is the bond between macro- and micro-scale, and  $T_M$  is used as the threshold to judge whether the computation goes on. The macro-phase  $\phi$  is used to depict the shape and position of the macro-product, and the micro-phase  $\varphi$  is used to depict the crystallization and decide the physical property.

#### IV. NUMERICAL RESULTS AND DISCUSSION

The proposed system is suitable for large-scale simulation. We achieve high efficiency by applying parallel computation on GPUs. Unless otherwise specified, we have chosen the following parameters for the simulation of additive manufacturing:  $Q = 9.62 \times 10^{-9} \text{ m}^3/\text{s}$ ,  $v_s = 0.1 \text{ m/s}$ ,  $A_s = 113$ ,  $B_s = 3440$ ,  $C_s = 203$ ,  $T_M = 293.15 \text{ K}$ ,  $\rho_1 = 1240 \text{ kg/m}^3$ ,  $\rho_2 = 0.9 \text{ kg/m}^3$ ,  $C_{p1} = 2000 \text{ J/kg K}$ ,  $C_{p2} = 1000 \text{ J/kg K}$ ,  $k_1 = 0.195 \text{ W/m K}$ ,  $k_2 = 0.034 \text{ W/m K}$ ,  $\lambda = 0.1$ ,  $\varepsilon = h$ .

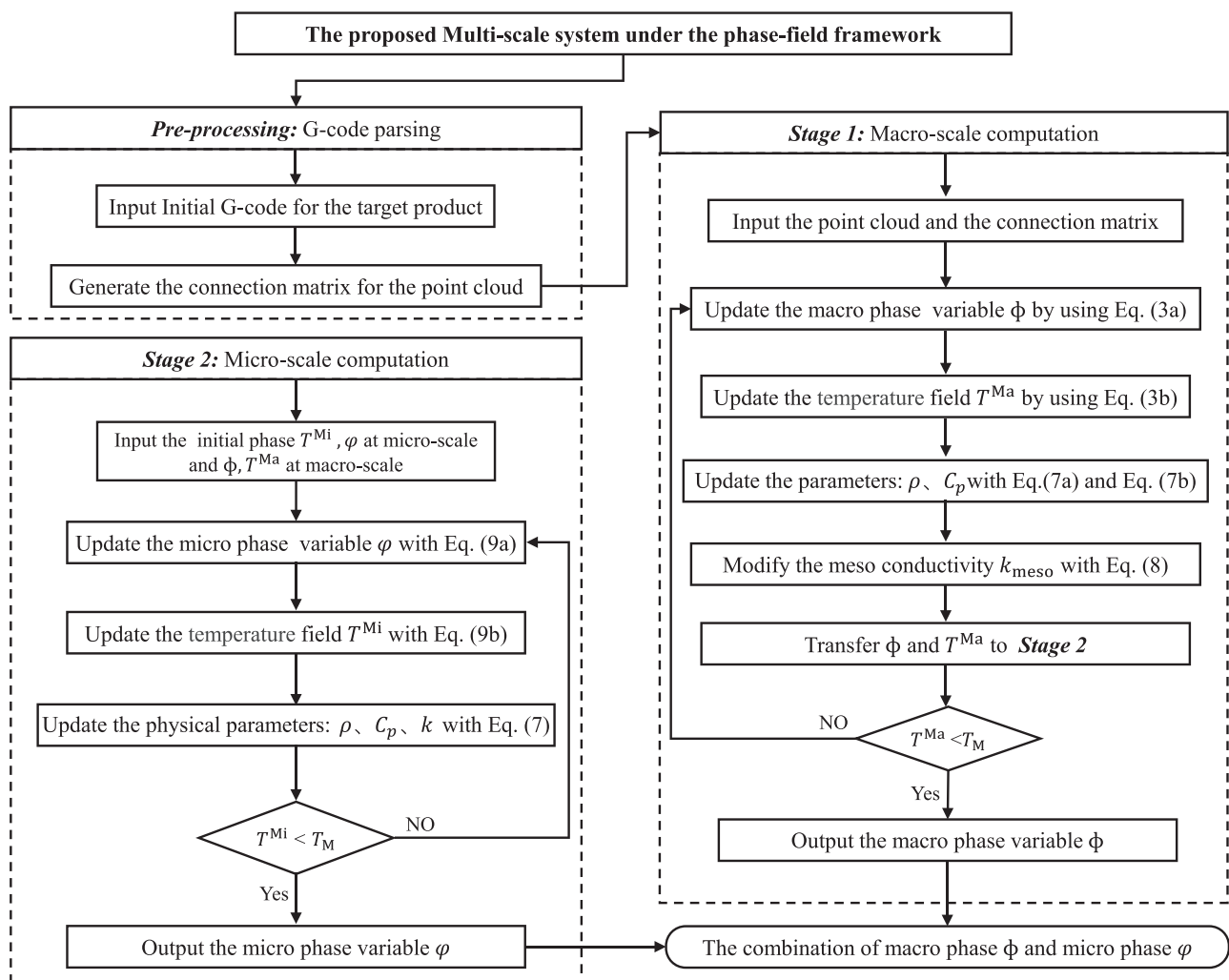
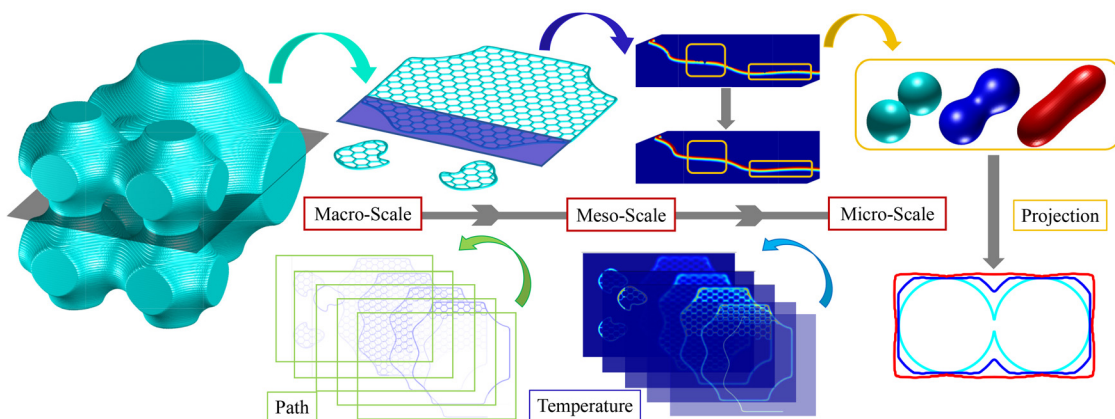


FIG. 2. The flow chart of the proposed multi-scale system for additive manufacturing based on the phase-field method.



**FIG. 3.** The schematic diagram of our proposed multi-scale model.

#### A. The proposed framework

Now, we address the schematic diagram of the proposed multi-scale model, which has been shown in Fig. 3. The investigated model is a modified periodic minimal surface model, which can be obtained from Ref. 50. We use a G-code generation algorithm<sup>51</sup> to design the movement trajectory of the printer nozzle. What stands out in this figure is the wide correlation between the multi-scale spaces. From left to right, these results show the 3D effect which can be obtained by our proposed model at the macro, meso, and micro-scales, respectively. At the beginning of this figure, the digital model with texture has been presented, which is the simulation of fused filament extrusion under the guidance of G-code. For the detailed detection of the smaller scale, we chose the middle slice of the numerical model. At the mesoscopic scale, we have demonstrated the evolution of the path and temperature field of the middle slice. In order to investigate the performance of microstructure in the process of silk spraying, we compared the phase transformation behavior by simulating the extrusion of the polymer

from the nozzle. Finally, the process of material fusion is explored from the microscopic point of view. It should be emphasized that, as shown in Fig. 3, our method does effectively establish a multi-scale computing framework, which corresponds to the physical context.

#### B. The comparison of the deposition with different temperatures

The temperature plays a significant role in filament deposition during the AM process. In order to investigate the influence of the bonding area in contact caused by heat diffusion, we apply the comparison of the deposition with different temperatures as shown in Fig. 4. The size of the computational domain is  $0.5 \times 0.5 \times 0.3 \text{ mm}^3$  with a resolution of  $512 \times 512 \times 308$  macro-mesh grid points and  $10 \times 10 \times 10 \mu\text{m}^3$  with a resolution of  $200 \times 200 \times 200$  micro-mesh grid points. To ignore the effect of deposition order on the results, we assume that the four initial droplets have the same physical morphology. The results obtained by  $T^{\text{Ma}} = 473.15$  and  $T^{\text{Ma}} = 573.15 \text{ K}$  have

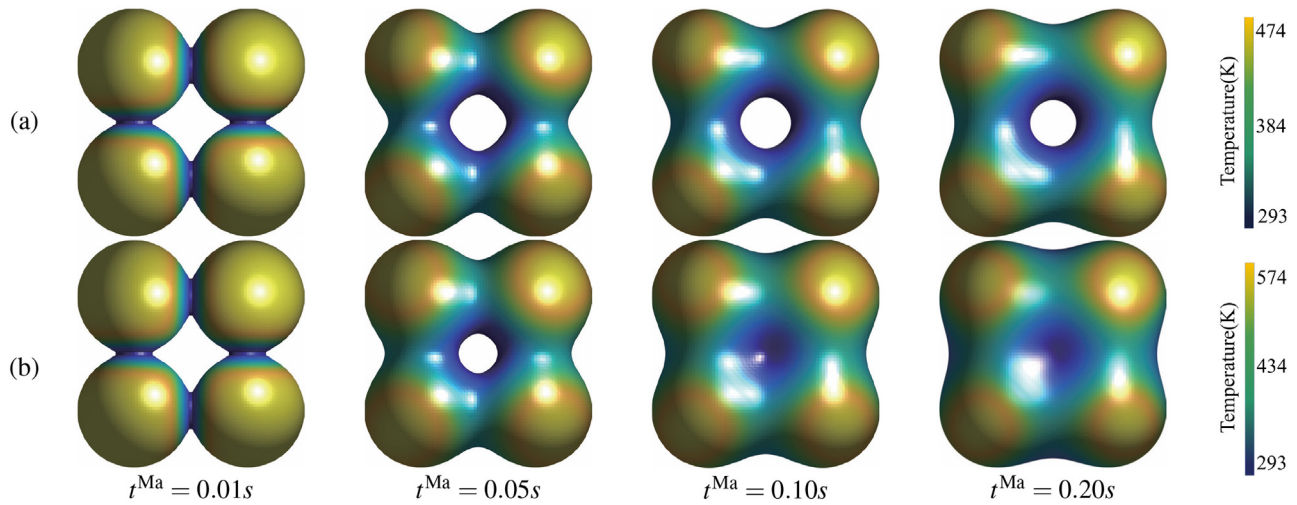


**FIG. 4.** The evolution of the deposition of filament with different temperature. (a) The deformation results with  $T = 473.15 \text{ K}$ , and (b) The deformation results with  $T = 573.15 \text{ K}$ . From left to right, the indicate times are  $t = 0.01, 0.05, 0.10$ , and  $0.20 \text{ s}$ , respectively.

been shown in Figs. 4(a) and 4(b), respectively. According to the evolution of the droplets deposition, we can obviously see that the merging effect is demonstrated between the droplets during the deposition and the heat diffuses above the composite structure. We should note that high temperature leads to huge deformation without considering the viscoelastic stress based on our model. In order to avoid nonphysical shape deformation, we unify the measures of digital and physical space so that our model can be directly applied to simulations by using real physical parameters according to the physics context.

### C. Modeling capability investigation with filaments under meso-scale framework

To demonstrate the capability for mesoscale simulation of the proposed model, we carry out the two-layer object with six filaments as shown in Fig. 5. The size of the computational domain is  $1.0 \times 1.0 \times 0.5$  mm<sup>3</sup> with a resolution of  $512 \times 512 \times 256$  macro-mesh grid points and  $10 \times 10 \times 10$  μm<sup>3</sup> with a resolution of  $200 \times 200 \times 200$  micro-mesh grid points. The top filaments are placed perpendicular to the bottom filaments. The closed view of the black windows shows the representative phenomena obtained by the proposed method. Some remarkable notations should be summarized as follows: (i) As can be seen from Fig. 5(a), the heat is distributed in a ladder form between two adjacent filaments, which is directly related to the direction and velocity of the nozzle. (ii) The heat is not evenly distributed in the filaments. The finished filaments continue to release heat during the solidification, which causes the temperature between the two filaments to be higher than that directly above as shown in Fig. 5(b). (iii) The

solidified filaments will remelt and glue to the new filament while the nozzle moves at high temperature as shown in Figs. 5(c) and 5(d). (iv) The heat diffuses radially and the high-temperature area is mainly concentrated in the interface between the second layer and the first layer which can be shown in Figs. 5(e) and 5(f). Spacing between neighboring filaments is required to reduce heat accumulation. Furthermore, we apply a comparison test from two-directional views of Figs. 5(c) and 5(f) as shown in Fig. 6. The purpose of this investigation is to explore the deformation trend of the filament during the simulated manufacturing process and how heat diffusion affects the contact area. Figure 6 can be interpreted as follows: Fig. 6(a) is the front view and Fig. 6(b) is the lateral view. The first column is the numerical simulation results and the second column is the comparison results by 0-contour lines of the cross-section. Based on the comparison results, we can clearly see that the neighboring parts of the first layer melt during the manufacturing process of the second layer as shown in the black windows. Although the filaments are partially melted, the height of the two-layer structure is still 2D, which does not bring numerical oscillation to the processing of the third-layer simulation.

### D. Investigation of the heat diffusion between different scales

In order to take the investigation of the heat diffusion between different scales, we simulate the manufacturing process of spiral-type modeling as shown in Fig. 7. The size of the computational domain is  $5.0 \times 4.6 \times 0.3$  mm<sup>3</sup> with a resolution of  $642 \times 590 \times 38$  macro-mesh grid points and  $10 \times 10 \times 10$  μm<sup>3</sup> with a resolution of

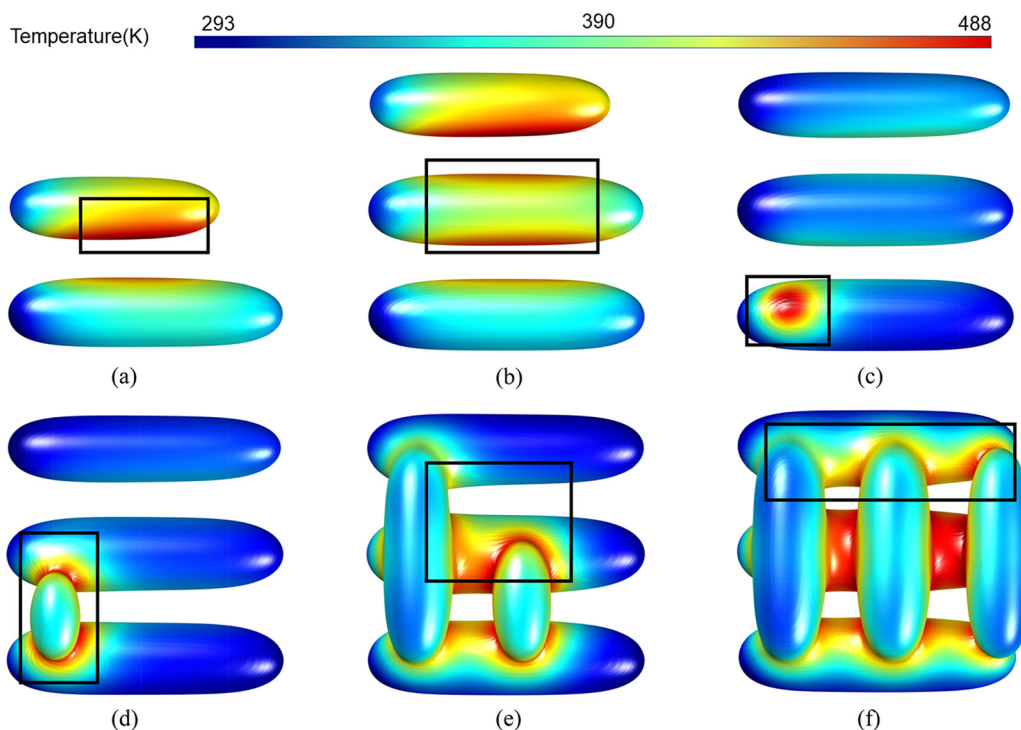


**FIG. 5.** The time evolution of the printing process with a two-layers object. The top filaments are placed perpendicular to the bottom filaments. From (a) to (f), the corresponding figure are captured at specific times. The closed view of the black windows shows the representative phenomena of the proposed method.

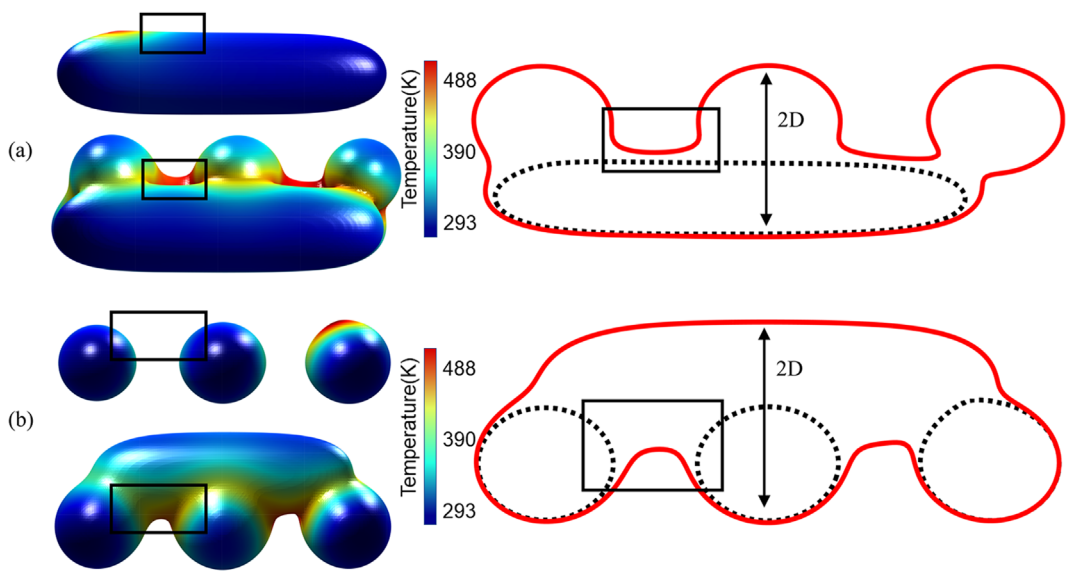


**FIG. 6.** Two directional views of Figs. 5(c) and 5(f): (a) Front view and (b) lateral view. The first column is the numerical simulation results, and the second column shows the comparison results by the 0-contour lines of the cross-section.

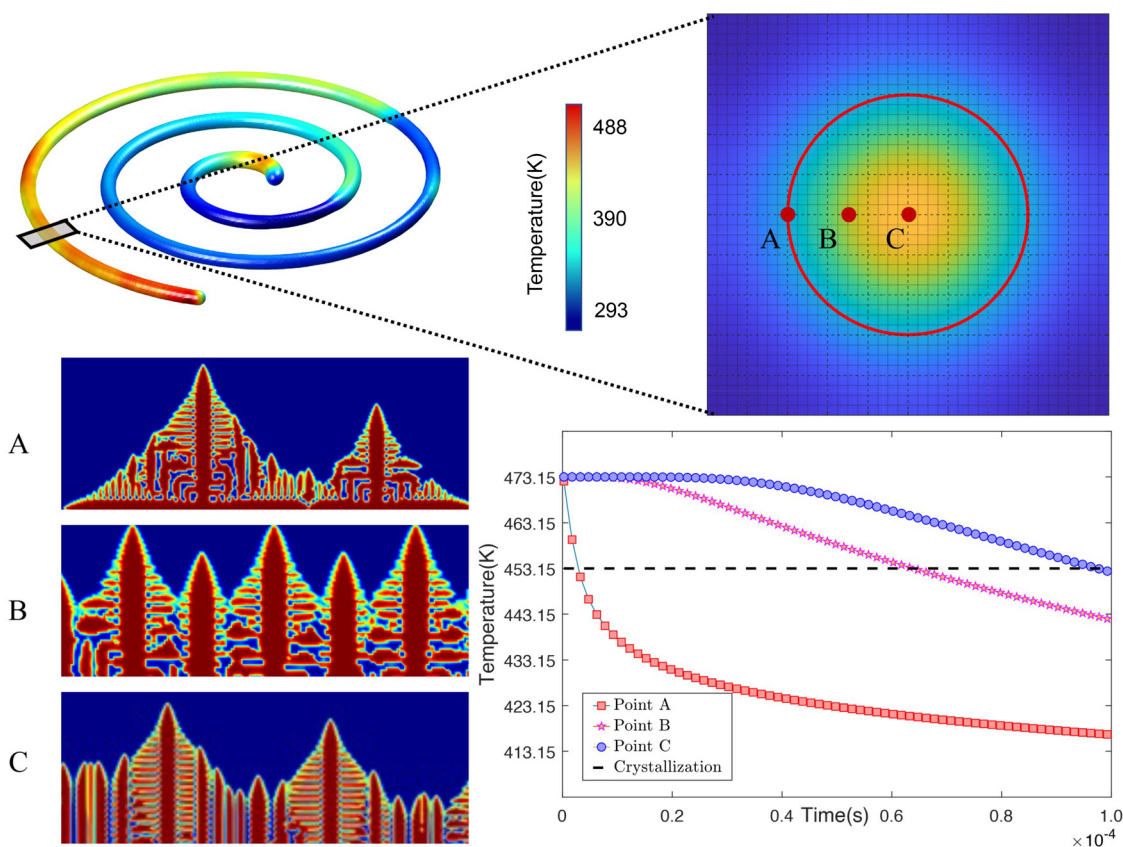


**FIG. 7.** Investigation of the heat diffusion between different scales. The top figures are the numerical simulation of injection filament and the temperature distribution of the cross-section. The bottom figures are the crystallization simulation at point A, B, and C, and their temperature trend at corresponding points, respectively.

$200 \times 200 \times 200$  micro-mesh grid points. We take a cross-section of the spiral model and show the temperature distribution at a specific time as shown in the second subfigure. The red line is the 0-contour line of the cross-section. By identifying the three fixed points A, B, and C in the computational domain, the temperature trend and crystal state at the three locations are shown in the bottom subfigures. It is clear that the temperature change on the surface of the filament is faster than that on the inside of the filament from the temperature change curve. The difference in temperature change leads to adaptive crystallization. As we expected, the proposed method takes the temperature field as the bond to couple the macro- and micro-scale computation.

### E. Parameter sensitivity analysis

To further explore the relationship between temperature and phase transformation with the deformation parameter  $\lambda$ , we compare

the results obtained with  $\lambda = 0.01, 0.1$ , and  $1$  in Fig. 8. The size of the considering object is  $40 \times 60 \times 0.4 \text{ mm}^3$  with a resolution of  $800 \times 1200 \times 12$  macro-mesh grid points and  $10 \times 10 \times 10 \mu\text{m}^3$  with a resolution of  $200 \times 200 \times 200$  micro-mesh grid points. It is obvious that the value of  $\lambda$  is positively correlated with the thickness of the filament. Since the larger volume leads to a larger area of contact between the filaments and the air, the heat diffuses faster. In other words, the increase in normalized average volume fraction is accompanied by the decrease in normalized average temperature. In Fig. 8(d), we compared the deformations of different  $\lambda$  in the microscopic scale. We use the bottom subfigure to demonstrate the comparison between the results obtained by different  $\lambda$ . It can be seen that the volume of crystallization is positively correlated with the value of  $\lambda$ , which implies that the micro- and macro-behaviors are consistent through the proposed model. We should note that the parameter  $\lambda$  is a dimensionless parameter, which is dependent on the properties of the materials such

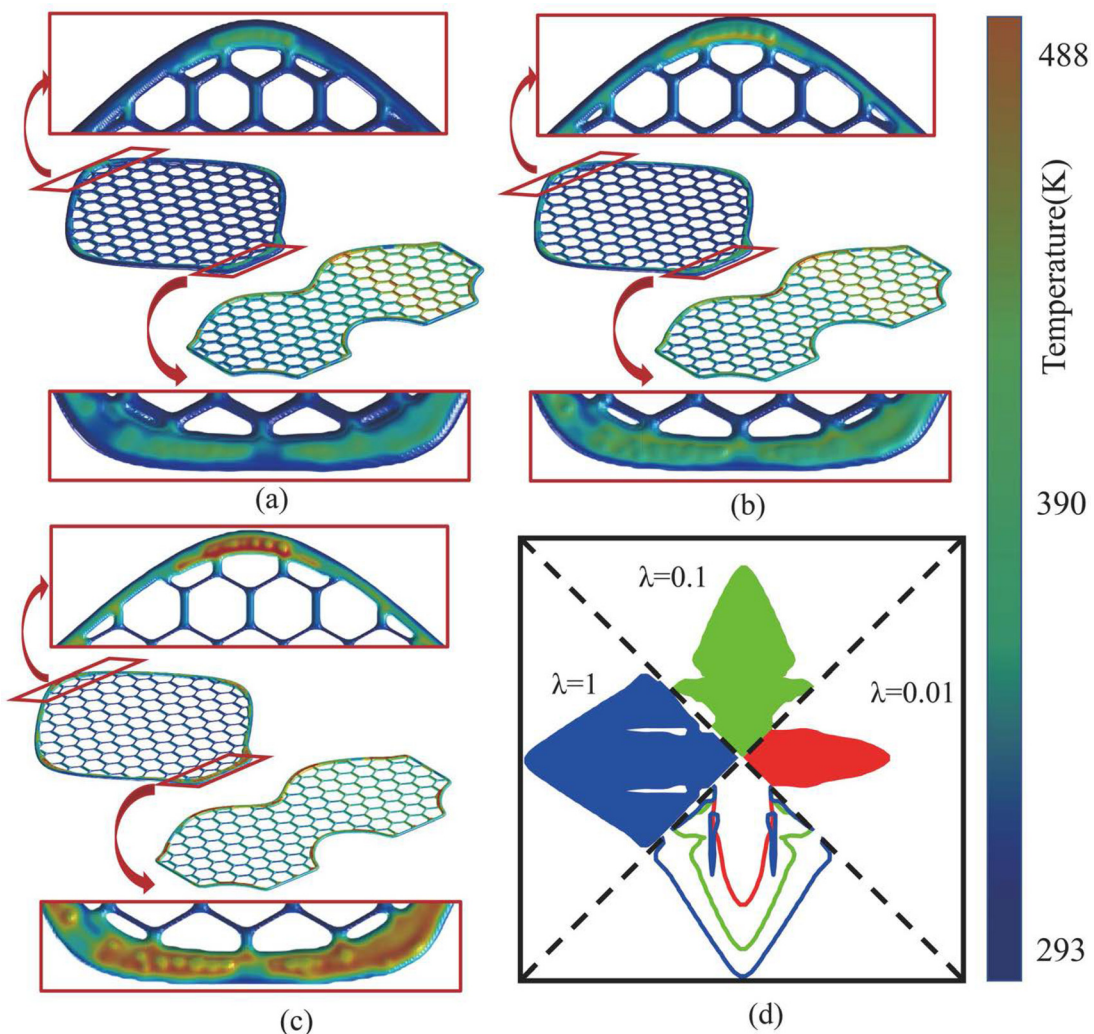


**FIG. 8.** The inquiry into the deformation coefficient  $\lambda$  in the model. From (a) to (c), the single-layer simulation obtained by  $\lambda = 1$ ,  $\lambda = 0.1$ , and  $\lambda = 0.01$ , respectively. (d) is the 2D comparison with different  $\lambda$  of microscopic crystals. The bottom subfigure is the combination of the 0-contour line of the three results.

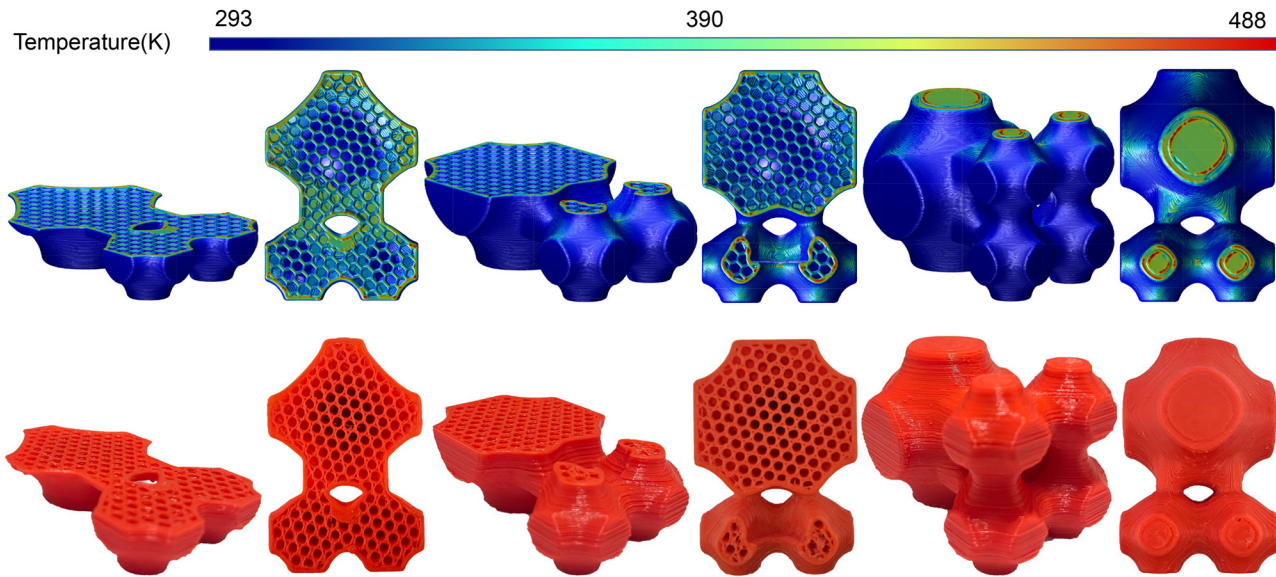


**FIG. 9.** Numerical simulation and additive manufacturing results at different stages. The top row is the digital model of temperature distribution on the surface. The bottom row is the additive manufacturing results with PLA material.

as density, viscosity, coefficient of thermal expansion, and Young's modulus and the manufacturing conditions such as nozzle temperature, ambient temperature, and the diameter of the filament, respectively. Thus, there is no analytic selection scheme for choosing parameter  $\lambda$  in our proposed method. However, we can provide a parameter interval  $\lambda \in (0, 1]$  to ensure the digital model maintains the physical characteristics.

#### F. The comparison between the numerical result with product of the additive manufacturing

In order to demonstrate how well our model captures the physics phenomena, we compare the numerical results with the product of AM at different stages as shown in Fig. 9. The first row demonstrates the digital model of temperature distribution on the surface. The second row is the AM results with PLA material. The 3D shape of the manufactured object is recorded by means of a high-resolution camera ( $2591 \times 1944$  pixels) at a frame rate of 2 fps. The size of the considering object is  $40 \times 60 \times 40$  mm $^3$  with a resolution of  $512 \times 768 \times 512$  macro-mesh grid points and  $10 \times 10 \times 10$   $\mu\text{m}^3$  with a resolution of  $200 \times 200 \times 200$  micro-mesh grid points. We comprehensively consider the influence of the macroscopic temperature field and the moving heat source. The observed results can be summarized as follows: (i) The heat is concentrated at the junction or the inflection point since the inflection point is the intersection of the nozzle track and the heat diffused along the filament. (ii) Considering the single-layer temperature field, the heat distribution is strongly correlated with the nozzle trajectory. Yet/However from a macro-point of view, the heat will dissipate and the temperature will approach the ambient temperature. (iii) The temperature simulation of the current layer is influenced not only by the moving heat source but also by the heat diffusion of the lower layer. Corresponding to expectations, the digital model of the proposed system is well-matched with the additive manufacturing

results. We should make some discussion on the multi-scale model corresponding to the AM process: (i) Our macro-scale model is constructed as the continuum model, which only considers heat transfer and convection and does not consider molten pool flow. In order to make the macro-scale simplified model have a solid physical basis to ensure certain accuracy, the simplification is based on the main conclusions obtained from the mesoscale model, including the equivalent heat transfer coefficient of the powder bed is also calculated by the mesoscale model, the equivalent energy absorption rate of the heat source model is the calculation result of the mesoscopic scale model used. (ii) The micro-scale model is used to investigate the properties of materials and mechanical performance by controlling the grain structure evolution and the microscopic residual stresses while having little influence on the deformation of the whole manufactured object. (iii) If we only use the macro-scale model without considering the microscopic and mesoscopic cases, we can obtain a digital model with a similar appearance and shape, but a lack of recognition of mesoscopic or microscopic defects. In other words, the single macro-scale model makes mathematical sense and is lack physical consistency.

#### V. CONCLUSION

In summary, this paper comprehensively considered temperature gradient, crystallization phenomenon, process parameters, and other factors in AM, and creatively proposed a multi-scale multi-physical field coupling model based on the FD technology. This model avoided single-scale consideration and numerically described the whole process of fused deposition with high temperature based on a global perspective. To the best of our knowledge, the study presented in this paper is one of the first investigations to project the real AM process to the virtual space with a physical model. Based on this model, the temperature distribution and shape change of the prepared parts can be simulated at the macro-scale, the filament fabrication can be

simulated at the mesoscale, and the thermal strain between materials and crystallization can be explored at the micro-scale. Compared with the existing physical model suitable for FD technology, different influences of heat transfer in multiple scales were fully considered and taken as the link to connect multiple physical fields in the digital-analog AM process.

The proposed model in this paper is the initial version of the corresponding digital model extracted from the additive manufacturing process. In future work, we will investigate the convective and radiative heat transfer between filaments, the influence of the dimensionless parameter  $\lambda$ , and the latent heat with the phase change to further refine the model. We will design a GPU parallel solver to speed up computation for the multi-scale model. In addition, we will conduct experiments such as anti-fatigue testing to further modify the mathematical model and feedback control the manufacturing process.

## ACKNOWLEDGMENTS

Y. Li is supported by National Natural Science Foundation of China (No. 12271430). Q. Xia is supported by the Fundamental Research Funds for the Central Universities, China (No. XYZ022022005). The authors would like to thank the reviewers for their constructive and helpful comments regarding the revision of this article.

## AUTHOR DECLARATIONS

### Conflict of Interest

The authors have no conflicts to disclose.

### Author Contributions

**Qing Xia:** Conceptualization (equal); Investigation (equal); Methodology (equal); Software (equal); Visualization (equal); Writing – original draft (equal). **Gangming Sun:** Conceptualization (equal); Writing – original draft (equal). **Junseok Kim:** Methodology (equal); Supervision (equal); Writing – review & editing (equal). **Yibao Li:** Conceptualization (equal); Methodology (equal); Project administration (equal); Software (equal); Supervision (equal); Writing – review & editing (equal).

## DATA AVAILABILITY

The data that support the findings of this study are available from the corresponding author upon reasonable request.

## REFERENCES

- <sup>1</sup>J. G. Michopoulos, A. P. Iliopoulos, J. C. Steuben, A. J. Birnbaum, and S. G. Lambrakos, “On the multiphysics modeling challenges for metal additive manufacturing processes,” *Addit. Manuf.* **22**, 784–799 (2018).
- <sup>2</sup>D. Gu, C. Ma, M. Xia, D. Dai, and Q. Shi, “A multiscale understanding of the thermodynamic and kinetic mechanisms of laser additive manufacturing,” *Engineering* **3**, 675–684 (2017).
- <sup>3</sup>Q. Chen, X. Liang, D. Hayduke, J. Liu, L. Cheng, J. Oskin, R. Whitmore, and A. C. To, “An inherent strain based multiscale modeling framework for simulating part-scale residual deformation for direct metal laser sintering,” *Addit. Manuf.* **28**, 406–418 (2019).
- <sup>4</sup>F. Liou, J. Newkirk, Z. Fan, T. Sparks, X. Chen, K. Fletcher, J. Zhang, Y. Zhang, K. S. Kumar, and S. Karnati, “Multiscale and multiphysics modeling of additive manufacturing of advanced materials,” NASA Langley Research Center Technical Report No. NASA/CR-2015-218691, 2015.
- <sup>5</sup>H. Xia, J. Lu, and G. Tryggvason, “A numerical study of the effect of viscoelastic stresses in fused filament fabrication,” *Comput. Methods Appl. Mech. Eng.* **346**, 242–259 (2019).
- <sup>6</sup>Q. Xia, J. Yang, and Y. Li, “On the conservative phase-field method with the N-component incompressible flows,” *Phys. Fluids* **35**, 012120 (2023).
- <sup>7</sup>Q. Xia, J. Kim, and Y. Li, “Modeling and simulation of multi-component immiscible flows based on a modified Cahn-Hilliard equation,” *Eur. J. Mech. B* **95**, 194–204 (2022).
- <sup>8</sup>Y. Li, R. Liu, Q. Xia, C. He, and Z. Li, “First- and second-order unconditionally stable direct discretization methods for multi-component Cahn-Hilliard system on surfaces,” *J. Comput. Appl. Math.* **401**, 113778 (2022).
- <sup>9</sup>W. Yan, J. Smith, W. Ge, F. Lin, and W. K. Liu, “Multiscale modeling of electron beam and substrate interaction: A new heat source model,” *Comput. Mech.* **56**, 265–276 (2015).
- <sup>10</sup>W. Yan, W. Ge, J. Smith, S. Lin, O. L. Kafka, F. Lin, and W. K. Liu, “Multi-scale modeling of electron beam melting of functionally graded materials,” *Acta Mater.* **115**, 403–412 (2016).
- <sup>11</sup>W. Yan, W. Ge, Y. Qian, S. Lin, B. Zhou, W. K. Liu, F. Lin, and G. J. Wagner, “Multi-physics modeling of single/multiple-track defect mechanisms in electron beam selective melting,” *Acta Mater.* **134**, 324–333 (2017).
- <sup>12</sup>W. Yan, S. Lin, O. L. Kafka, Y. Lian, C. Yu, Z. Liu, J. Yan, S. Wolff, H. Wu, E. Ndip-Agbor *et al.*, “Data-driven multi-scale multi-physics models to derive process-structure-property relationships for additive manufacturing,” *Comput. Mech.* **61**, 521–541 (2018).
- <sup>13</sup>Z. Wang, W. Yan, W. K. Liu, and M. Liu, “Powder-scale multi-physics modeling of multi-layer multi-track selective laser melting with sharp interface capturing method,” *Comput. Mech.* **63**, 649–661 (2019).
- <sup>14</sup>M. Liu and G. Liu, *Particle Methods for Multi-Scale and Multi-Physics* (World Scientific, 2015).
- <sup>15</sup>M. Markl and C. Körner, “Multiscale modeling of powder bed-based additive manufacturing,” *Annu. Rev. Mater. Sci.* **46**, 93–123 (2016).
- <sup>16</sup>R. Geng, J. Du, Z. Wei, G. Zhao, and J. Ni, “Multiscale modeling of microstructural evolution in fused-coating additive manufacturing,” *J. Mater. Eng. Perform.* **28**, 6544–6553 (2019).
- <sup>17</sup>Y. Li, Q. Xia, C. Lee, S. Kim, and J. Kim, “A robust and efficient fingerprint image restoration method based on a phase-field model,” *Pattern Recognit.* **123**, 108405 (2022).
- <sup>18</sup>Q. Xia, G. Sun, Q. Yu, J. Kim, and Y. Li, “Thermal-fluid topology optimization with unconditional energy stability and second-order accuracy via phase-field model,” *Commun. Nonlinear Sci. Numer. Simul.* **116**, 106782 (2023).
- <sup>19</sup>S. Vyawahare, S. Teraiya, D. Panghal, and S. Kumar, “Fused deposition modeling: A review,” *Rapid Prototyping J.* **26**, 176–201 (2020).
- <sup>20</sup>O. A. Mohamed, S. H. Masood, and J. L. Bhowmik, “Optimization of fused deposition modeling process parameters: A review of current research and future prospects,” *Adv. Manuf.* **3**, 42–53 (2015).
- <sup>21</sup>H. Xia, J. Lu, S. Dabiri, and G. Tryggvason, “Fully resolved numerical simulations of fused deposition modeling—Part I: Fluid flow,” *Rapid Prototyping J.* **24**, 463–476 (2018).
- <sup>22</sup>T. Rahim, A. Abdullah, and H. Akil, “Recent developments in fused deposition modeling-based 3D printing of polymers and their composites,” *Polym. Rev.* **59**, 589–624 (2019).
- <sup>23</sup>A. Sheoran and H. Kumar, “Fused deposition modeling process parameters optimization and effect on mechanical properties and part quality: Review and reflection on present research,” *Mater. Today* **21**, 1659–1672 (2020).
- <sup>24</sup>S. Wasti and S. Adhikari, “Use of biomaterials for 3D printing by fused deposition modeling technique: A review,” *Front. Chem.* **8**, 315 (2020).
- <sup>25</sup>Q. Yu, Q. Xia, and Y. Li, “A phase field-based systematic multiscale topology optimization method for porous structures design,” *J. Comput. Phys.* **466**, 111383 (2022).
- <sup>26</sup>H. Huang, N. Ma, J. Chen, Z. Feng, and H. Murakawa, “Toward large-scale simulation of residual stress and distortion in wire and arc additive manufacturing,” *Addit. Manuf.* **34**, 101248 (2020).
- <sup>27</sup>S. Nelaturi, W. Kim, and T. Kurtoglu, “Manufacturability feedback and model correction for additive manufacturing,” *CRP J. Manuf. Sci. Technol.* **137**, 021015 (2015).
- <sup>28</sup>D. Wang and X. Chen, “Closed-loop high-fidelity simulation integrating finite element modeling with feedback controls in additive manufacturing,” *J. Dyn. Syst. Meas. Control* **143**, 021006 (2021).

- <sup>29</sup>A. Nasirov, S. Hasanov, I. Fidan *et al.*, “Prediction of mechanical properties of fused deposition modeling made parts using multiscale modeling and classical laminate theory,” in Proceedings of the 30th Annual International Solid Freeform Fabrication Symposium—An Additive Manufacturing Conference, Austin, TX (2019), Vol. 1376.
- <sup>30</sup>L. Sánchez-Balanzar, F. Velázquez-Villegas, L. Ruiz-Huerta, and A. Caballero-Ruiz, “A multiscale analysis approach to predict mechanical properties in fused deposition modeling parts,” *Int. J. Adv. Manuf. Technol.* **115**, 2269–2279 (2021).
- <sup>31</sup>H. Xia, J. Lu, and G. Tryggvason, “Simulations of fused filament fabrication using a front tracking method,” *Int. J. Heat Mass Transfer* **138**, 1310–1319 (2019).
- <sup>32</sup>H. Xia, J. Lu, and G. Tryggvason, “Fully resolved numerical simulations of fused deposition modeling—Part II: Solidification, residual stresses and modeling of the nozzle,” *Rapid Prototyp. J.* **24**, 973–987 (2018).
- <sup>33</sup>Q. Xia, Q. Yu, and Y. Li, “A second-order accurate, unconditionally energy stable numerical scheme for binary fluid flows on arbitrarily curved surfaces,” *Comput. Methods Appl. Mech. Eng.* **384**, 113987 (2021).
- <sup>34</sup>Y. Li, K. Wang, Q. Yu, Q. Xia, and J. Kim, “Unconditionally energy stable schemes for fluid-based topology optimization,” *Commun. Nonlinear Sci. Numer. Simul.* **111**, 106433 (2022).
- <sup>35</sup>Y. Li, L. Zhang, Q. Xia, Q. Yu, and J. Kim, “An unconditionally energy-stable second-order time-accurate numerical scheme for the coupled Cahn–Hilliard system in copolymer/homopolymer mixtures,” *Comput. Mater. Sci.* **200**, 110809 (2021).
- <sup>36</sup>C. McIlroy and R. Graham, “Modelling flow-enhanced crystallisation during fused filament fabrication of semi-crystalline polymer melts,” *Addit. Manuf.* **24**, 323–340 (2018).
- <sup>37</sup>M. Francois, A. Sun, W. King, N. Henson, D. Tourret, C. Bronkhorst, N. Carlson, C. Newman, T. Haut, J. Bakosi, J. Gibbs, V. Livescu, S. Wiel, A. Clarke, M. Schraad, T. Blacker, H. Lim, T. Rodgers, S. Owen, F. Abdeljawad, J. Madison, A. Anderson, J. Fattebert, R. Ferencz, N. Nodge, S. Khairallah, and O. Walton, “Modeling of additive manufacturing processes for metals: Challenges and opportunities,” *Curr. Opin. Solid State Mater. Sci.* **21**, 198–206 (2017).
- <sup>38</sup>Y. Li, K. Qin, Q. Xia, and J. Kim, “A second-order unconditionally stable method for the anisotropic dendritic crystal growth model with an orientation-field,” *Appl. Numer. Math.* **184**, 512–526 (2023).
- <sup>39</sup>J. Langer, “Models of pattern formation in first-order phase transitions,” in *Directions in Condensed Matter Physics: Memorial Volume in Honor of Shang-Keng Ma* (World Scientific, 1986), pp. 165–186.
- <sup>40</sup>H. G. Lee and J. Kim, “An efficient and accurate numerical algorithm for the vector-valued Allen–Cahn equations,” *Comput. Phys. Commun.* **183**, 2107–2115 (2012).
- <sup>41</sup>Y. Li and J. Kim, “Phase-field simulations of crystal growth with adaptive mesh refinement,” *Int. J. Heat Mass Transfer* **55**, 7926–7932 (2012).
- <sup>42</sup>X. Tong, C. Beckermann, A. Karma, and Q. Li, “Phase-field simulations of dendritic crystal growth in a forced flow,” *Phys. Rev. E* **63**, 061601 (2001).
- <sup>43</sup>X. Huang, X. Tian, Q. Zhong, S. He, C. Huo, Y. Cao, Z. Tong, and D. Li, “Real-time process control of powder bed fusion by monitoring dynamic temperature field,” *Adv. Manuf.* **8**, 380–391 (2020).
- <sup>44</sup>M. Jamshidinia, F. Kong, and R. Kovacevic, “Numerical modeling of heat distribution in the Electron Beam Melting of Ti-6Al-4V,” *J. Manuf. Sci. Eng.* **135**, 061010 (2013).
- <sup>45</sup>A. Karma and W. Rappel, “Phase-field method for computationally efficient modeling of solidification with arbitrary interface kinetics,” *Phys. Rev. E* **53**, R3017 (1996).
- <sup>46</sup>A. Barbieri and J. Langer, “Predictions of dendritic growth rates in the linearized solvability theory,” *Phys. Rev. A* **39**, 5314 (1989).
- <sup>47</sup>A. Karma and W. Rappel, “Quantitative phase-field modeling of dendritic growth in two and three dimensions,” *Phys. Rev. E* **57**, 4323 (1998).
- <sup>48</sup>M. Dodd and A. Ferrante, “A fast pressure-correction method for incompressible two-fluid flows,” *J. Comput. Phys.* **273**, 416–434 (2014).
- <sup>49</sup>X. Yang, “Efficient linear, stabilized, second-order time marching schemes for an anisotropic phase field dendritic crystal growth model,” *Comput. Methods Appl. Mech. Eng.* **347**, 316–339 (2019).
- <sup>50</sup>Y. Li, Q. Xia, S. Yoon, C. Lee, B. Lu, and J. Kim, “Simple and efficient volume merging method for triply periodic minimal structures,” *Comput. Phys. Commun.* **264**, 107956 (2021).
- <sup>51</sup>A. Brown and D. Beer, “Development of a stereolithography (STL) slicing and G-code generation algorithm for an entry level 3-D printer,” in *2013 Africon* (IEEE, 2013), pp. 1–5.